Electronic Supplementary Material (ESI) for Nanoscale.

Supporting Information: Optical properties of orthorhombic germanium sulfide: Unveiling the Anisotropic Nature of Wannier Exciton

Mehdi Arfaoui,[*,†] Natalia Zawadzka,[‡] Sabrine Ayari,[¶] Zhaolong Chen,[§,‖] Kenji Watanabe,[⊥] Takashi Taniguchi,[#] Adam Babiński,[‡] Maciej Koperski,[§,‖] Sihem Jaziri,[†] and Maciej R. Molas[*,‡]

†*Laboratoire de Physique de la Matière Condensée, Département de Physique, Faculté des Sciences de Tunis, Université Tunis El Manar, Campus Universitaire 1060 Tunis, Tunisia.*

‡*Institute of Experimental Physics, Faculty of Physics, University of Warsaw, Warsaw, Poland.*

¶*Laboratoire de Physique de l'Ecole normale supérieure, ENS, Université PSL, CNRS, Sorbonne Université, Université de Paris, 24 rue Lhomond, 75005 Paris, France.*

§*Institute for Functional Intelligent Material, National University of Singapore, 117575, Singapore.*

‖*Department of Materials Science and Engineering, National University of Singapore, 117575, Singapore.*

⊥*Research Center for Electronic and Optical Materials, National Institute for Materials Science, 1-1 Namiki, Tsukuba 305-0044, Japan*

#*Research Center for Materials Nanoarchitectonics, National Institute for Materials Science, 1-1 Namiki, Tsukuba 305-0044, Japan*

E-mail: mehdi.arfaoui@fst.utm.tn; maciej.molas@fuw.edu.pl

Contents

A Supporting experimental results

A.1 Polarization-resolved reflectance contrast spectra of GeS

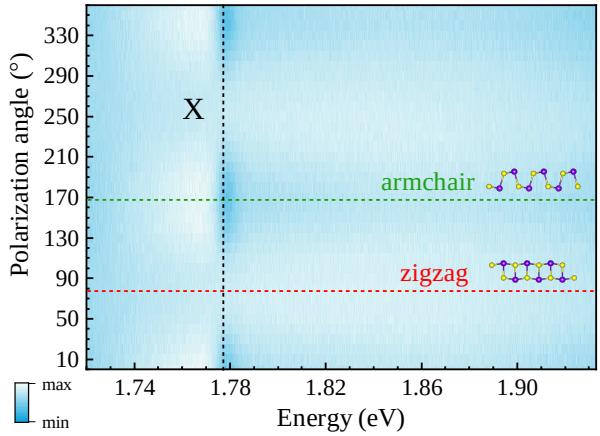

Figure S1: False-colour map of the low-temperature (T=5 K) polarization-resolved RC spectra measured on the GeS encapsulated in h-BN flakes.

Figure S1 shows the low-temperature (T=5 K) polarization-resolved reflectance contrast (RC) spectra measured on the GeS encapsulated in h-BN flakes. In contrast to the several emission lines observed in the corresponding PL spectra shown in Figures S2 and S3, the RC spectra consist of a single resonance. Furthermore, its energy of about 1.78 eV coincides with the X emission line. The polarization dependence of the X resonance indicates that this transition is linearly polarized along the armchair direction, as well as its emission counterpart (see Figure S3). The obtained RC results confirm that the energetically lowest optical transitions in GeS are dominated by a direct transition polarized along the armchair direction.

A.2 The influence of excitation energy on the PL spectra of GeS

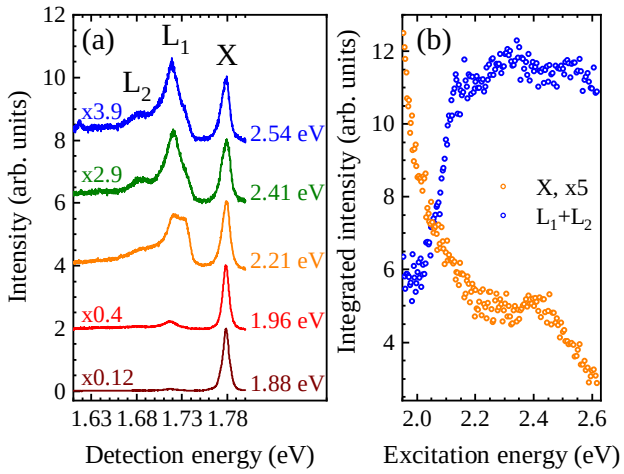

Figure S2: (a) The low-temperature (T=5 K) PL spectra of the investigated GeS encapsulated in h-BN flakes under five different excitation energies, denoted in the figure. (b) The integrated intensities of the free (X) and localized (L_1 and L_2) excitons as a function of excitation energy. Note that the X intensity was multiplied 5 times for clarity.

As we found that the encapsulation energy can strongly affect the L_1 and L_2 intensities (compare Figure 1(c) in the main text and the one reported in Ref.[1]), we performed measurements of the low-temperature PL spectra of the GeS encapsulated in the h-BN flakes under five different excitation energies, see Figure S2(a). The modification of the laser energy causes two main effects: (i) The emission intensity of the X line is significantly reduced by around 30 times with the change of the excitation energy from 1.88 eV to 2.54 eV. While the 1.88 eV excitation is possible only around the Γ point of the Brillouin zone (BZ), the high energy 2.54 eV one may involve transitions originating from different points of the BZ, see Figure 5(a) in the main text. (ii) The relative intensity of the emission lines due to the localized (L_1 and L_2) and free (X) excitons is also substantially modified when excitation is changed. To investigate this effect in detail, we measured PL excitation (PLE) spectra. Figure S2 presents the integrated intensities of the free (X) and localized (L_1 + L_2) excitons as a function of the excitation energy in the energy range from about 1.97 eV to 2.63 eV. The measured PLe spectra of the X and L_1 + L_2 are analogous to their behaviour shown

in panel (a) of the Figure. The emission intensity of the X line experiences a monotonic reduction of more than 4 times. Simultaneously, the L_1 + L_2 intensity is enhanced twice when the excitation energy is increased from 1.97 eV to about 2.15 eV, and then stays almost at the same level. It suggests that at illuminations higher than 2.15 eV, the excited carriers are subjected to more nonradiative processes, which leads to an increase in probability of the L_1 and L_2 emission, see Figure 5(a) in the main text. Note that when we combine the results obtained in panels (a) and (b) of Figure S2, the extraordinary reduction of the X intensity in transition from 1.88 eV to 2.63 eV excitation is on the order of 50 times, which is accompanied by an increase in the intensity of L_1 + L_2.

A.3 The polarization and temperature evolutions of the PL spectra of GeS under the 2.41 eV excitation

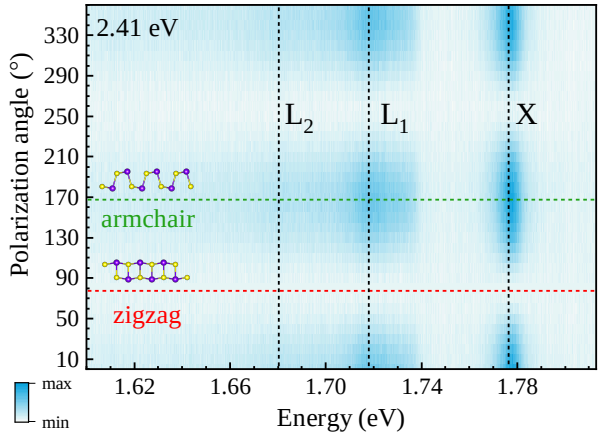

Figure S3: False-colour map of the low-temperature (T=5 K) polarization-resolved PL spectra measured on the GeS encapsulated in h-BN flakes under excitation of 2.41 eV. Note that the intensity scale is linear.

To investigate the origin of the L_1 and L_2 emission lines, we measured the polarization and temperature evolutions of the low-temperature (T=5 K) PL spectra of the GeS encapsulated in h-BN flakes under excitation of 2.41 eV, see Figures S3 and S4. The choice of excitation energy is motivated by the relatively high intensity of the L_1 and L_2 peaks under this laser

energy compared to others, see Figure S2. As can be seen in Figure S3, the L_1 and L_2 lines are linearly polarized along the same armchair direction as the neutral exciton transition. Moreover, with increasing temperature, the low-energy L_1 and L_2 peaks quickly disappear from the PL spectra, see Figure S4(a). At T=60 K, only the X emission contributes to the PL spectrum, which is seen up to 130 K. The possibility of the X observation at smaller temperature range, only to 130 K under the 2.41 eV excitation versus 190 K under the 1.88 eV, can be understood in terms of the significant decrease in the X intensity when the excitation energy increases (see Figure S2). The temperature dependence of the X line leads to the typical redshift and the linewidth broadening at higher temperatures, which is presented in Figures. S4(b) and (c) with the corresponding fitted curves. The temperature evolutions of the energy and the linewidth of the X line are characterized using the Odonnell[2] and Rudin[3] relations, introduced in the main text. We use the same values of phonon related parameters, i.e., $< \hbar\omega >$=26 meV and $\hbar\omega$=30 meV, while the other parameters were free. The fitted curves reproduce quite well the experimental data. Note that the observed temperature dependence of the L lines is very similar to the previously reported behavior of the so-called "localized" excitons in monolayers of WS_2 and WSe_2 exfoliated on Si/SiO_2 substrates.[4,5]

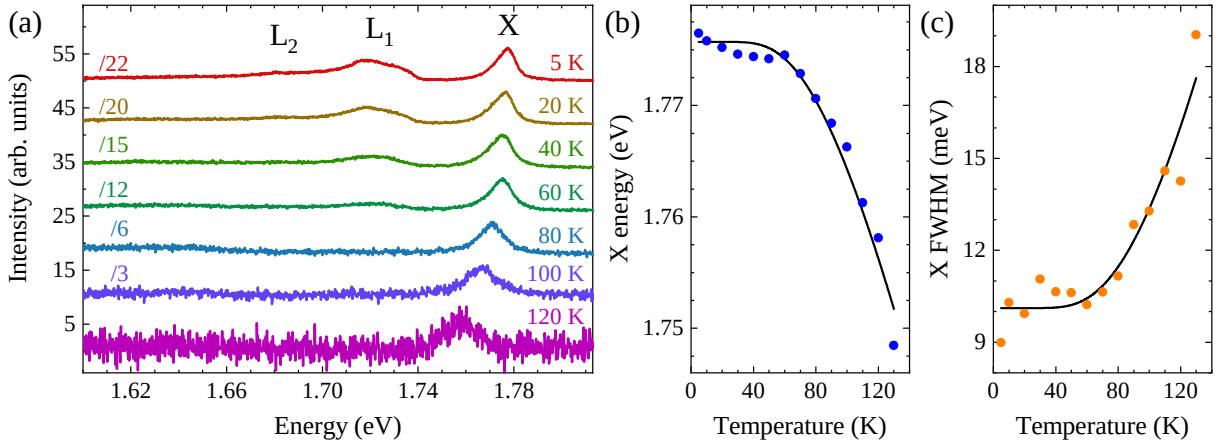

Figure S4: (a) The temperature-dependent PL spectra measured on the GeS flake with 2.41 eV laser light excitation. The spectra are vertically shifted and are divided by scaling factors for clarity. The determined (b) energy and (c) full width at half maximum (FWHM) of the neutral exciton (X) line. The circles represent the experimental results while the curves are fits to the data obtained with the aid of Eq. 1 and 2, described in the main text.

B Identification of low energy peaks in GeS

In addition to the free neutral exciton peak located around 1.78 eV (see Figure S3), at low temperature (T=5 K), PL measurements proved the existence of multiple emission peaks on GeS flake, which are located about 60-100 meV, below the neutral exciton. The nature and origin of these low-energy emission bands remain unknown from both theoretical and experimental considerations. Different scenarios can be discussed to identify some of those peaks: i) exciton plus negative trion (X_-) and its fine structure; ii) exciton plus biexciton (XX) and auger recombination process; iii) exciton plus an optical phonon replica; and iv) exciton plus a localized state.

Starting by testing the assumption that the lower state is an emission of charged excitons (X_-) and it's a fine structure. In the presence of residual charges, the Coulomb interaction could further bind an electron or hole to an exciton to form a charged exciton (negative and/or positive, depending on the doping conditions). X_- appears frequently in 2D TMDs,[6,7] phosphorus,[8,9] and CdSe platelets.[10] In the absorption and emission spectra, X_- and its fine structure are observed at energies lower than those of the neutral excitons.[6,7] Typically, the binding energy (BE) of a charged exciton, i.e., the energy difference between X and X_- is very small compared to the exciton BE,[10–12] so it is difficult to observe it in semi-3D conductors, which require low temperatures and very high-quality crystals. To form an X_- complex, the excess carrier added to the generated exciton has to stem from an ionized exciton from the previous laser pulse. Thus, the very low excitation density used rules out an efficient X_- generation. Among the options considered for the lower states, L_j, is a Biexciton (XX). An XX complex is a bound state of two electrons and two holes. It is often described approximately as the bound state of two excitons, where the interaction between the excitons is treated as a perturbation.[13,14] This approximation is justified if the BE of XX (the energy difference between the two free excitons and the XX) is much smaller than that of the exciton.

An agreement against XXs is the low excitation density $50\mu W/cm^{-2}$ used in our PL

measurements, as Poisson statistics result in a negligible probability for absorption of two photons within one laser pulse. In addition to XX and X$_-$ fine structure, two other possible mechanisms including exciton–phonon interaction and defect-related scattering can be discussed to give a reasonable explanation for these exceptional multiple emission peaks in the spectra.

Starting with the phonon replicas. The D_{2h}^{16} space group gives rise to 24 vibrational modes. Their representation in the center of the zone is: $\Gamma = 4A_g + 2B_{1g} + 4B_{2g} + 2B_{3g} + 2A_u + 4B_{1u} + 2B_{2u} + 4B_{3u}$. There are seven infrared-active phonons and twelve Raman-active phonons. Raman and infrared modes are split as a result of interlayer interactions.[1] A replica phonon of the exciton peak at E_{L_1} is one of the options available for the low-peaks. Excitons with a large wavevector $\boldsymbol{K}$ can recombine if a phonon or several phonons are involved that provide the necessary momentum $\boldsymbol{q} = \boldsymbol{K}_1 - \boldsymbol{K}_2$, with $\boldsymbol{K}_1$ ($\boldsymbol{K_2}$) being the wavevector of the initial (intermediate) exciton state. The so-called *zero-phonon* line at energy $E_{\tilde{1s}}^X$ is then accompanied by a phonon replica below $E_{\tilde{1s}}^X$ at integer multiples of the optical phonon energy $\hbar\omega_{ph}$ with energy $E_n = E_{\tilde{1s}}^X - n\hbar\omega_{ph}$. This presumption can only be proved if the exciton and the induced replica phonon peak have the same dynamic properties. In Figure S2(a,b), we experimentally investigated the effect of excitation energy on the PL spectra and we found that the exciton peak and the low emission line L_1 and L_2 have different behavior as a function of the excitation energy, which can be an argument against the replica phonon nature of those low-lying peaks, since it is expected that they follow the same trend as the main exciton peak, as both are related to the excitonic transition.

Finally, we test the assumption that the lower states L_1 and L_2 are localized excitons. As a result of thermal equilibrium and the kinetics of processing, all real materials contain structural imperfections that could significantly affect their properties.[15–17] In fact, structural defects such as residual impurities, vacancies, adatoms, interstitials, and anti-sites,[15–19] often introduce rich luminescent properties in semiconductor materials. When photo-excited electron-hole pairs are trapped in a disorder potential, which may be created by lattice de-

fects, localized states may form within the band gap (BG) with an emission energy below the exciton. In temperature-dependent PL spectroscopy measurements (see Figure S4), these low emission peaks were observed at relatively low temperatures ($T < 60K$), in such a way that they vanish faster than the exciton as a function of temperature. A possible explanation is that, as compared with exciton, these peaks have smaller BEs, which can be termalized more easily with increasing temperatures. In fact, at low temperatures, a certain amount of carriers could be captured by these localized, trapped states. As the temperature increased, the trapped carriers could be released again from the localized states and recombine radiatively, leading to the increased PL intensity of the exciton. Furthermore, the dependence of the L_1 and L_2 peak on the excitation energy (in Figure S2(a, b)) suggests the presence of an effective exciton "mobility edge", i.e., below (above) a certain energy, the center-of-mass motion of the excitons is localized (delocalized).[20] Depending on this qualitatively study, exciton localized state is the most likely mechanism. The latter has also been widely used for explaining the low-energy peak in PL spectroscopy in TMDs and traditional semiconductor materials. However, our understanding of the fundamental properties of the multiple emission lines in GeS remains incomplete. These suggested possible mechanisms still need to be systematically addressed theoretically and experimentally, which is beyond the scope of this article.

C Independent Particle Approximation for Linear Optical Response

In the independent particle approximation (IPA), the diagonal elements of the imaginary part of the dielectric tensor in the long-wavelength limit are basically given by [21]

$$\begin{aligned}\varepsilon_{2_{i,i}}(\omega) = &\underbrace{\frac{4\pi e^2}{\Omega N_{\mathbf{k}} m^2} \sum_{n} \sum_{\mathbf{k}\in BZ} \frac{df\left(E_{\mathbf{k},n}\right)}{dE_{\mathbf{k},n}} \frac{\eta\omega \mathbf{M}_{i,i}^{c,v}(\mathbf{k})}{\omega^4 + \eta^2\omega^2}}_{\text{Intraband}} \\ &+ \underbrace{\frac{8\pi e^2}{\Omega N_{\mathbf{k}} m^2} \sum_{n_c \neq n_v} \sum_{\mathbf{k}\in BZ} \frac{\mathbf{M}_{i,i}^{c,v}(\mathbf{k})}{E_{\mathbf{k},n_c} - E_{\mathbf{k},n_v}} \frac{\gamma\omega f\left(E_{\mathbf{k},n_v}\right)}{\left[\left(\omega_{\mathbf{k},n_c} - \omega_{\mathbf{k},n_v}\right)^2 - \omega^2\right]^2 + \gamma^2\omega^2}}_{\text{Interband}},\end{aligned} \tag{S1}$$

while the real part comes from the Kramers-Kronig transformation, which reads

$$\begin{aligned}\varepsilon_{1_{i,i}}(\omega) = 1 &- \underbrace{\frac{4\pi e^2}{\Omega N_{\mathbf{k}} m^2} \sum_{n} \sum_{\mathbf{k}\in BZ} \frac{df\left(E_{\mathbf{k},n}\right)}{dE_{\mathbf{k},n}} \frac{\omega^2 \mathbf{M}_{i,i}^{c,v}(\mathbf{k})}{\omega^4 + \eta^2\omega^2}}_{\text{Intraband}} \\ &+ \underbrace{\frac{8\pi e^2}{\Omega N_{\mathrm{k}} m^2} \sum_{n_v \neq n_c} \sum_{\mathrm{k}\in BZ} \frac{\mathbf{M}_{i,i}^{c,v}(\mathbf{k})}{E_{\mathrm{k},n_c} - E_{\mathbf{k},n_v}} \frac{\left[\left(\omega_{\mathrm{k},n_c} - \omega_{\mathrm{k},n_v}\right)^2 - \omega^2\right] f\left(E_{\mathrm{k},n_v}\right)}{\left[\left(\omega_{\mathrm{k},n_c} - \omega_{\mathrm{k},n_v}\right)^2 - \omega^2\right]^2 + \gamma^2\omega^2}}_{\text{Interband}}\end{aligned} \tag{S2}$$

where γ and η are the broadening of the interband and intraband transitions, respectively. $\mathbf{M}_{i,i}^{c,v}(\mathbf{k})$ is the squared optical transition dipole matrix elements (OME), where $\mathbf{k}$ is the single particle wavevector. The OME, $\mathbf{M}_{i,i}^{c,v}(\mathbf{k})$, obtained by the density functional theory (DFT) calculation and determines the optical strength of a transition. Furthermore, it contains all symmetry-imposed selection rules. Ω is the volume of the lattice cell, n_v and n_c belong correspondingly to the valence and conduction bands, $E_{\mathbf{k},n}$ are the eigenvalues, and $f(E_{\mathbf{k},n})$ is the Fermi distribution function that accounts for the occupation of the bands with band index n. The derivative of the Fermi distribution function for interband transitions, described by the first sum in Eq. S1 and Eq. S2, is substantially zero, except in the region close to the Fermi level.

D GW method and Bethe-Salpeter Equation

The Bethe-Salpeter equation (BSE) is calculated on top of the GW eigenvalues. Conduction band energies are rigidly shifted by the GW correction, although valence band energies are barely affected. Therefore, the effective masses of the hole and electron states do not differ between DFT and GW. Based on the Kohn–Sham wavefunctions and the quasi-particles correction, the optical spectra are derived at the level of the BSE using the following equation[22]

$$\left(E^{QP}_{c\mathbf{k}} - E^{QP}_{v\mathbf{k}}\right) A^{S}_{vc\mathbf{k}} + \sum_{\mathbf{k}'v'c'} \langle vc\mathbf{k} \left| K_{eh} \right| v'c'\mathbf{k}' \rangle \, A^{S}_{v'c'\mathbf{k}'} = \Omega^{S} A^{S}_{vc\mathbf{k}}, \tag{S3}$$

where $E^{QP}_{c\mathbf{k}}$ and $E^{QP}_{v\mathbf{k}}$ are the quasiparticle energies of the valence and conduction band states obtained with the GW method, respectively. A^{S}_{vck} and Ω^{S} correspond to the exciton eigenstates and eigenvalues of the S^{th} exciton. The electron-hole interaction kernel, K_{eh}, contains the exchange interaction V (repulsive) and the screened Coulomb interaction W (attractive). The imaginary part of the dielectric function $\varepsilon_2(\hbar\omega)$ is calculated from the excitonic states as follows[23]

$$\varepsilon_2(\hbar\omega) \propto \sum_{S} \left| \sum_{cv\mathbf{k}} A^{S}_{vc\mathbf{k}} \frac{\langle c\mathbf{k} \left| \mathbf{p}_i \right| v\mathbf{k} \rangle}{\varepsilon_{c,\mathbf{k}} - \varepsilon_{v,\mathbf{k}}} \right|^2 \delta\left(\Omega^{S} - \hbar\omega - \gamma\right), \tag{S4}$$

where $\langle c\mathbf{k} \left| \mathbf{p} \right| v\mathbf{k} \rangle$ are the dipole matrix elements of the transitions from the valence bands to the conduction bands. γ is the broadening energy. In the main text, the exciton weight represented in k-space is defined as follows $w(\mathbf{k}) = \sum_{n_\mathbf{t}} \left| \mathbf{A}_{n_\mathbf{t}\mathbf{k}} \right|^2$, which sums over transitions at each $\mathbf{k}$ point. In addition, The electron-hole (e-h) excited state is represented by the expansion[22]

$$\left| S \right\rangle = \sum_{c}^{e} \sum_{v}^{h} \sum_{\mathbf{k}} A_{vc\mathbf{k}} \left| vc\mathbf{k} \right\rangle. \tag{S5}$$

From the solution of the BSE, we obtain the coefficients $A_{vc\mathbf{k}}$. Representation of this function is usually done by fixing the hole position and representing the exciton density as a function of the electron position.

The single-shot G_0W_0 method commonly used in computational physics to calculate the electronic properties of solid systems. However, the technique sometimes produces unsatisfactory results because of its reliance on the DFT-starting point, resulting in a BG that is insufficiently small compared to the experimental one. To overcome this issue, we used the self-consistency of GW only on eigenvalues (evGW), which improves the accuracy of the calculation. It involves an iterative calculation of evGW up to four times, ensuring that the difference between consistent GW values is 0.01 eV, ultimately leading to convergence of the BG, see Figure S5.

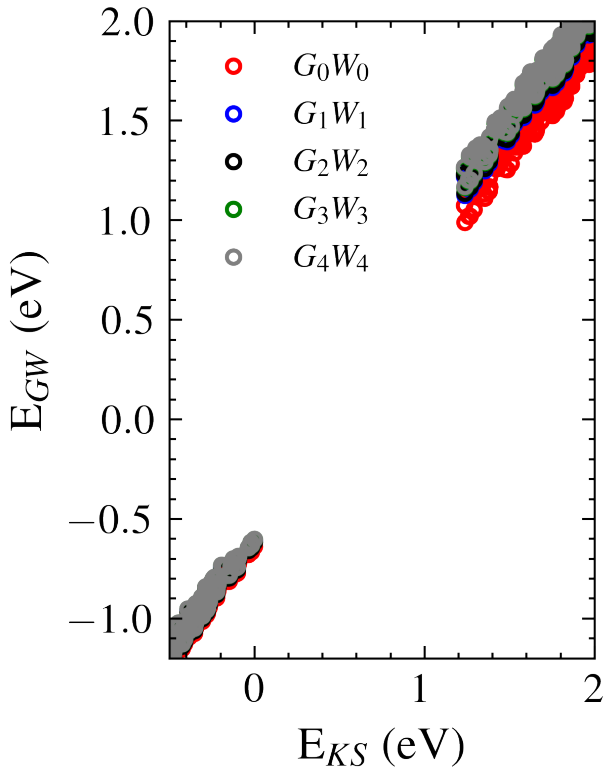

Figure S5: Quasi-particle bandgap calculation: Scissor operator correction in QP and renormalization of conduction and valence bands.

E Projected Density of States of GeS

The projected fatband density of states (PDOS) can be calculated by projecting the wavefunctions onto the atomic orbitals. The resulting fatband PDOS, presented in Figure S6,

provides information on the distribution of the electronic states of GeS. Each band is assigned a color that represents the s-, p-, and d-orbitals. We report the PDOS on both the Ge and S atoms, as depicted in Figure S6(a)-(f). The obtained results demonstrate that the valence (conduction) states are contributed predominantly by S (Ge) atoms, with significant contributions of p-orbital. These results align well with previous theoretical predictions reported in the Refs.[24–26]

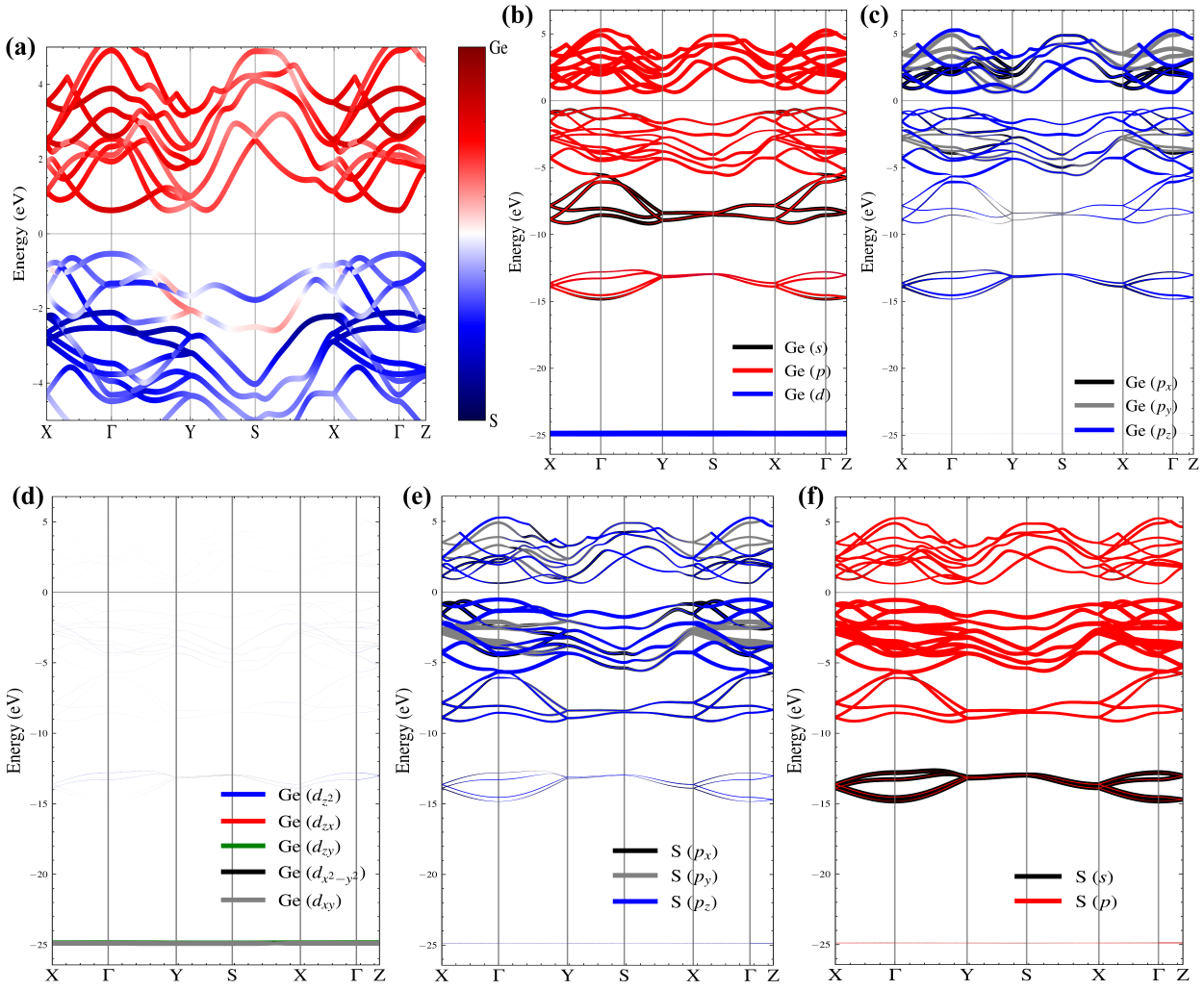

Figure S6: **Electronic band structures with orbital projections for GeS**. The orbital projections are depicted with varying radii, with the size of the colored circles representing the relative weight of the orbital contributions to the electronic states.

F Anisotropic Wannier exciton theory within the effective mass approximation

Different methods have been used to calculate the optical properties of exciton states in semiconductor nanostructures, such as the variational method,[27–29] *ab-initio* calculations based on GW+BSE,[30,31] and the effective mass theory (EMA).[32–34] The variational method has limitations and is typically used to calculate low-energy states, making it less powerful than alternative methods for higher-energy states. The ab-initio calculations are an accurate way to calculate the exciton states. However, they are computationally expensive and it is difficult to systematically study some effects by varying a few phenomenological parameters. The EMA has the advantage of performing simple and fast computational procedures to accurately calculate the ground and excited states. Moreover, we were able to systematically study the effect of the anisotropy on the optical properties of the exciton in GeS, which helps us to more intuitively understand the role of excitonic effects. The anisotropy of excitons in GeS is of great importance for both fundamental research and device applications.

Here, we employ a variationally optimized diagonalization method based on a hydrogenic basis to calculate the properties of the exciton states in bulk GeS. To dig deeper into the excitonic anisotropy in such crystals, we used the EMA. The Hamiltonian that describes the exciton anisotropy can be written as follows

$$\mathbf{H}_X = \sum_{i=x,y,z} \frac{{\mathbf{P_{i,e}}}^2}{2\, m_{eff}^{e,i}} + \sum_{i=x,y,z} \frac{{\mathbf{P_{i,h}}}^2}{2\, m_{eff}^{h,i}} + \mathbf{V}_{Coul}(|\mathbf{r_e} - \mathbf{r_h}|), \tag{S6}$$

where the momentum operator $\mathbf{P}_{\mathbf{i},\nu} = -i\hbar\boldsymbol{\nabla}_{i,\nu}$; $(i = x, y, z)$. $m_{eff}^{\nu,i}$ is the effective mass of the electron ($\nu = \mathrm{e}$) and the hole ($\nu = \mathrm{h}$) in different directions i. $\mathbf{r}_\nu = (x_\nu, y_\nu, z_\nu)$ are the position vectors of the electron and hole. $\mathbf{V}_{Coul}(|\mathbf{r_e} - \mathbf{r_h}|)$ represents the Coulomb interaction between the electron and hole screened by the background dielectric constants ε_i of the anisotropic semiconductor. Excitonic properties in bulk semiconductors differ from those in monolayers

of the same material. In 2D materials, such as TMDs and black phosphorus, excitons are strongly confined, and dielectric screening is reduced, leading to non-hydrogenic Rytova-Keldysh potentials.[35–39] In contrast, bulk excitons are less confined and less sensitive to the dielectric environment. Our previous work[1] showed that the low-temperature (T=5 K) emission due to the free excitons measured on the GeS exfoliated on the SiO_2/Si substrate is similar to those reported here, which is obtained for the GeS encapsulated in the h-BN flakes. This indicates that excitonic optical properties in bulk GeS are independent of the dielectric environment. As such, e-h interactions in 3D homogeneous dielectric environments can be well described by the Coulomb potential. Using the relative and center-of-mass (COM) coordinates,

$$\mathbf{r} = \begin{cases} x = x_e - x_h, \\ y = y_e - y_h, \\ z = z_e - z_h, \end{cases} , \mathbf{R}_{CM} = \begin{cases} X_{CM} = \dfrac{m_{eff}^{e,x} x_e + m_{eff}^{h,x} x_h}{m_{eff}^{e,x} + m_{eff}^{h,x}}, \\ Y_{CM} = \dfrac{m_{eff}^{e,y} y_e + m_{eff}^{h,y} y_h}{m_{eff}^{e,y} + m_{eff}^{h,y}}, \\ Z_{CM} = \dfrac{m_{eff}^{e,z} z_e + m_{eff}^{h,z} z_h}{m_{eff}^{e,z} + m_{eff}^{h,z}}, \end{cases} . \tag{S7}$$

The Hamiltonian in Eq. S6 can be separated in COM and relative motion $\mathbf{H}_X = \mathbf{H}_X^{CM} + \mathbf{H}_X^{rel}$. The free COM motion of the exciton is described by

$$\mathbf{H}_X^{CM} = -\frac{\hbar^2 \boldsymbol{\nabla}_{X_{CM}}^2}{2\, M_{X,x}} - \frac{\hbar^2 \boldsymbol{\nabla}_{Y_{CM}}^2}{2\, M_{X,y}} - \frac{\hbar^2 \boldsymbol{\nabla}_{Z_{CM}}^2}{2\, M_{X,z}}, \tag{S8}$$

where $M_{X,i} = m_{eff}^{e,i} + m_{eff}^{h,i}$ denotes the exciton mass in direction i.

The relative motion of the exciton can be described by the following Schrödinger equation

$$\left[-\frac{\hbar^2}{2} \Big(\frac{1}{\mu_x} \frac{\partial^2}{\partial x^2} + \frac{1}{\mu_y} \frac{\partial^2}{\partial y^2} + \frac{1}{\mu_z} \frac{\partial^2}{\partial z^2} \Big) - \frac{e^2}{\sqrt{\varepsilon_y \varepsilon_z x^2 + \varepsilon_x \varepsilon_z y^2 + \varepsilon_x \varepsilon_y z^2}} \right] \boldsymbol{\Psi}_{\tilde{n},\tilde{\ell},\tilde{m}}^{rel}(\mathbf{r}) = E_{\tilde{n},\tilde{\ell},\tilde{m}}^{rel} \boldsymbol{\Psi}_{\tilde{n},\tilde{\ell},\tilde{m}}^{rel}(\mathbf{r}), \tag{S9}$$

where $E_{\tilde{n},\tilde{\ell},\tilde{m}}^{rel}$ represents the relative eigenvalue and $\boldsymbol{\Psi}_{\tilde{n},\tilde{\ell},\tilde{m}}^{rel}(\boldsymbol{r})$ are the corresponding eigenfunctions. Here, $\mu_i = (m_{eff}^{e,i} m_{eff}^{h,i})/(m_{eff}^{e,i} + m_{eff}^{h,i})$ is the reduced mass of the exciton along

the direction i and e is the electron charge. ε_i is the dielectric constant in the direction i.

If we change the variable ($x,\ y,\ z,$) into $(\xi, \eta, \zeta) = \left(\sqrt{\frac{\mu_x}{\bar{\mu}}}\, x,\ \sqrt{\frac{\mu_y}{\bar{\mu}}}\, y,\ \sqrt{\frac{\mu_z}{\bar{\mu}}}\, z\right)$, and if we define the anisotropy parameters $A = \dfrac{\bar{\mu}}{\mu_x}\dfrac{\varepsilon_y\varepsilon_z}{\bar{\varepsilon}^2}$, $B = \dfrac{\bar{\mu}}{\mu_y}\dfrac{\varepsilon_x\varepsilon_z}{\bar{\varepsilon}^2}$ and $C = \dfrac{\bar{\mu}}{\mu_z}\dfrac{\varepsilon_x\varepsilon_y}{\bar{\varepsilon}^2}$,[40] we obtain the following equation:

$$\mathbf{H}_X^{rel} = -\frac{\hbar^2}{2\bar{\mu}}\left(\frac{\partial^2}{\partial\xi^2} + \frac{\partial^2}{\partial\eta^2} + \frac{\partial^2}{\partial\zeta^2}\right) - \frac{e^2}{\bar{\varepsilon}\sqrt{A\xi^2 + B\eta^2 + C\zeta^2}}, \tag{S10}$$

where the anisotropy is now concentrated in the potential instead of the kinetic term. The anisotropy parameters A, B, and C are supposed to be real and positive.

$$\frac{1}{\bar{\mu}} = \frac{\bar{\varepsilon}}{3}\left(\frac{1}{\varepsilon_x\mu_x} + \frac{1}{\varepsilon_y\mu_y} + \frac{1}{\varepsilon_z\mu_z}\right), \bar{\varepsilon} = \sqrt[3]{\varepsilon_x\varepsilon_y\varepsilon_z} \tag{S11}$$

are the average-reduced mass and the average-dielectric constant, respectively. We treat the problem in spherical coordinates, where $\rho = \sqrt{\xi^2 + \eta^2 + \zeta^2}$.

When an isotropic Coulomb potential is integrated into the Hamiltonian, the resultant relative Hamiltonian, $\mathbf{H}_X^{rel}$, can be decomposed into two distinct components $\mathbf{H}_X^{rel} = \mathbf{H}_{hyd} + \mathbf{H}_{per}$. The first term is the unperturbed Hamiltonian $\mathbf{H}_{hyd}$, which has a spherical symmetry and defines the effective 3D hydrogenic Hamiltonian. The eigenstates of $\mathbf{H}_{hyd}$ are exact and correspond to the 3D hydrogenic eigenenergies $E_n = -\bar{R}_y/n^2$ and eigenfunction[33]

$$\mathbf{\Phi}_{n,\ell,m}(\boldsymbol{\rho}, \theta, \phi) = \sqrt{\left(\frac{2}{na_b}\right)^3 \frac{(n-\ell-1)!}{2n(n+\ell)!}}\, e^{-\frac{\boldsymbol{\rho}}{na_b}} \left(\frac{2\boldsymbol{\rho}}{na_b}\right)^{\ell} \mathbf{L}_{n-\ell-1}^{2l+1}\left(\frac{2\boldsymbol{\rho}}{na_b}\right) \mathbf{Y}_{\ell}^{m}(\theta, \phi), \tag{S12}$$

where $\mathbf{Y}_\ell^m(\theta, \phi)$ is the spherical harmonic function. $\mathbf{L}_\beta^\alpha$ is the generalized Laguerre polynomials. $a_b = \frac{\bar{\varepsilon}\hbar^2}{\bar{\mu}e^2}$ is the $3D$-exciton effective Bohr radius and $\bar{R}_y = \frac{e^4\bar{\mu}}{2\,\bar{\varepsilon}^2\hbar^2}$ is the $3D$-effective Rydberg energy. In this notation, n, ℓ and m are the principal, the azimuthal, and the magnetic quantum number, respectively. The degeneracy of the states is quantified as n^2-fold. The labeling convention for these states, according to their ℓ, is as follows: s for $\ell = 0$, p for $\ell = 1$, and d for $\ell = 2$. The spherical coordinate representation of the perturbed

Hamiltonian, $\mathbf{H}_{per}$, is expressed as

$$\mathbf{H}_{per} = \frac{e^2}{\bar{\varepsilon}\boldsymbol{\rho}}\left(1 - \frac{1}{\sqrt{\left(A\cos(\phi)^2 + B\sin(\phi)^2\right)\sin(\theta)^2 + C\cos(\theta)^2}}\right). \tag{S13}$$

The unperturbed Hamiltonian belongs to the infinite group of isotropic space, which is invariant under all symmetry operations. The perturbation reduces the symmetry of the system, leads to increase the degeneracy. The original problem of solving $\mathbf{H}_X^{rel}$ is now transformed into a matrix diagonalization problem, where the corresponding components are $\langle \mathbf{\Phi}_{n,\ell,m} | \mathbf{H}_X^{rel} | \mathbf{\Phi}_{n,\ell,m} \rangle$ and the basis $\mathbf{B}_{n,\ell,m} = \{\Phi_{n,\ell,m}(\boldsymbol{\rho},\theta,\phi), n \in \mathbf{N}^*, 0 \leq \ell \leq n-1, -\ell \leq m \leq \ell\}$. To evaluate the magnitude order of the perturbation, in the following, we compute the perturbed matrix elements $E^{per}_{\substack{n,\ell,m \\ n',\ell',m'}}$ for different states

$$E^{per}_{\substack{n,\ell,m \\ n',\ell',m'}}(A,B,C) = \langle \Phi_{n,\ell,m} | \mathbf{H}_{per} | \Phi_{n',\ell',m'} \rangle = -\bar{R}_y \, G_{\substack{n,\ell \\ n',\ell'}} \left(\mathbf{F}_{\substack{\ell,m \\ \ell',m'}}(A,B,C) + \mathbf{H}_{\substack{\ell,m \\ \ell',m'}} \right) \tag{S14}$$

where the integral of the radial part is given by

$$G_{\substack{n,\ell \\ n',\ell'}} = \int_0^\infty R_{n\ell}(\boldsymbol{\rho}) \cdot R_{n'\ell'}(\boldsymbol{\rho}) \cdot \rho \, \mathrm{d}\rho. \tag{S15}$$

In particular, if $n = n'$

$$G_{\substack{n,\ell \\ n',\ell'}} = \frac{1}{2n^2}\left[\delta_{\ell,\ell'} + \left(\frac{(n-\ell)(n-\ell+1)}{(n+\ell)(n+\ell-1)}\right)^{1/2} \delta_{\ell,\ell'+2}\right]. \tag{S16}$$

The angular part is given by the following two matrix elements

$$\mathbf{H}_{\substack{\ell,m \\ \ell',m'}} = \int_0^{2\pi}\int_0^{\pi} \mathbf{Y}_{\ell'}^{m'}(\theta,\phi)\mathbf{Y}_{\ell}^{m}(\theta,\phi)^* sin(\theta) d\theta d\phi = \delta_{\ell,\ell'}\delta_{m,m'}, \tag{S17}$$

$$\mathbf{F}_{\substack{\ell,m \\ \ell',m'}}(A,B,C) = \int_0^{2\pi}\int_0^{\pi} \frac{\mathbf{Y}_{\ell'}^{m'}(\theta,\phi)\mathbf{Y}_{\ell}^{m}(\theta,\phi)^* sin(\theta)d\theta d\phi}{\sqrt{\big(Acos^2(\phi)+Bsin^2(\phi)\big)sin^2(\Theta)+Ccos^2(\theta)}}, \tag{S18}$$

where $\mathbf{F}_{\ell,m,\ell',m'}(A,B,C)$ depend on the anisotropic parameters and on the angular quantum numbers ℓ, m, ℓ' and m'. The diagonalization of the Hamiltonian matrix constructed from the anisotropic coulomb potential leads to the following eigenstates $\mathbf{\Psi}^{rel}_{\tilde{n},\tilde{\ell},\tilde{m}}(\boldsymbol{\rho},\theta,\phi) = \sum_{n,\ell,m} C_{n,\ell,m}\mathbf{\Phi}_{n,\ell,m}(\boldsymbol{\rho},\theta,\phi)$ where the coefficients $C_{n,\ell,m}$ are obtained by solving the matrix problem. The subscripts on the coefficient $C_{n,\ell,m}$ noted $\tilde{n}$,$\tilde{\ell}$, and $\tilde{m}$ refers now to the dominant contribution of the coefficients to the excitonic function, corresponding to the coefficient of the highest weight. In the actual numerical calculations, the number of basis functions $\mathbf{B}_{n,\ell,m}$ should be finite. The basis functions are usually chosen, provided that they are the low-lying energy states of the Hamiltonian. We have computed eigenvalues and eigenfunctions that extend the basic set of wavefunctions until convergence is reached. To achieve the necessary precision for calculating the ground state energy and to ensure system convergence in our numerical computations, we considered hydrogen states with principal quantum numbers, n, up to 15 along with their corresponding orbital quantum numbers. The numerical procedure becomes stable for $n = 5$. The solutions of the resulting Schrödinger equation of the system satisfy the eigenequation

$$\Big(\mathbf{H}_X^{CM} + \mathbf{H}_X^{\text{rel}}\Big)\mathbf{\Upsilon}_{\tilde{n},\tilde{\ell},\tilde{m}}(\mathbf{R}_{CM},\boldsymbol{\rho}) = E^X_{\tilde{n},\tilde{\ell},\tilde{m}}\mathbf{\Upsilon}_{\tilde{n},\tilde{\ell},\tilde{m}}(\mathbf{R}_{CM},\boldsymbol{\rho}) \tag{S19}$$

are given by the eigenfunction

$$\mathbf{\Upsilon}_{\tilde{n},\tilde{\ell},\tilde{m}}(\mathbf{R}_{CM},\boldsymbol{\rho}) = \mathbf{\Phi}^{CM}(\mathbf{R}_{CM})\mathbf{\Psi}^{rel}_{\tilde{n},\tilde{\ell},\tilde{m}}(\boldsymbol{\rho}) \tag{S20}$$

and the eigenvalue

$$E^{X}_{\tilde{n},\tilde{\ell},\tilde{m}}(\mathbf{K}) = E_g^{GW} - E^{B}_{\tilde{n},\tilde{\ell},\tilde{m}} + \sum_{i=x,y,z} \frac{\hbar^2 \mathbf{K}_i^2}{2\, M_{X,i}}, \tag{S21}$$

where $E^{B}_{\tilde{n},\tilde{\ell},\tilde{m}} = -E^{rel}_{\tilde{n},\tilde{\ell},\tilde{m}}$ is the exciton BE. $\mathbf{\Phi}^{CM}(\mathbf{R}_{CM}) = \frac{1}{\sqrt{V}} \exp^{i\mathbf{R}_{CM}\mathbf{K}}$ is COM wavefunction. $E_g^{GW} = E_c^{QP} - E_v^{QP}$ and $\mathbf{K} = (K_x, K_y, K_z)$ denote the QP BG and COM wavevector, respectively. $V = N\Omega$ is the volume of bulk semiconductors. N and Ω represent the total number of primitive cells in the crystal and the volume of the unit cell, respectively. The exciton has an energy dispersion as a function of the COM wavevector $\mathbf{K}$, which describes the translational motion of an exciton with quasi-momentum $\hbar\mathbf{K}$. Thus, only the exciton with $\mathbf{K} = 0$ can recombine by emitting a photon, which is termed a coherent exciton. Consequently, excitons with $\mathbf{K} \neq 0$ cannot recombine directly to emit a photon and therefore are dark excitons. However, recombination emission for $\mathbf{K} \neq 0$ (in particular incoherent excitons) is possible and can be generated by a further phonon-assisted process, which we call an indirect transition. In the following section, since we are considering coherent optical excitation of excitons by photons, the excited excitons are predominantly those with zero COM momenta.

Once the exciton energy and wave functions have been obtained by diagonalizing the Hamiltonian, using the dipole matrix elements relevant to interband optical transitions, in this section we calculate the oscillator strength (OS) of the free neutral exciton. Because we work at low temperatures and under low-density excitation, we do not consider thermalization processes. The light-matter interaction in the Coulomb gauge under low-density excitation can be described by the Hamiltonian as follows[41]

$$H_{\text{opt}} = \frac{e\mathbf{A}(\mathbf{r}) \cdot \mathbf{p}}{m_0 c} \tag{S22}$$

where $\mathbf{p}$ is the electron momentum operator, e is the elementary charge. In the Fock repre-

sentation, the vector potential operator in the second quantization can be written as

$$\boldsymbol{A}_{\mathbf{q}}(\mathbf{r},t)=\mathbf{A}_{\mathbf{q}}(\mathbf{r})e^{-i\omega_{\mathbf{q}}t}+\mathbf{A}_{\mathbf{q}}^{+}(\mathbf{r})e^{i\omega_{\mathbf{q}}t} \tag{S23}$$

with

$$\mathbf{A}_{\mathbf{q}}(\mathbf{r})=\sqrt{\frac{2\pi\hbar c}{n_0\mathbf{q}V}}\times\boldsymbol{\alpha}_{\mathbf{q}}e^{i\mathbf{qr}}a_{\mathbf{q}} \tag{S24}$$

The operator $a_{\mathbf{q}}^{+}\,(a_{\mathbf{q}})$ creates (annihilates) a photon with the wavevector $\mathbf{q}$. $\boldsymbol{\alpha}_{\mathbf{q}}$ denotes the photon polarization unit vector. The optical angular frequency is defined by $\omega_{\mathbf{q}}=\frac{c}{n_0}|\mathbf{q}|$, where n_0 is the effective optical refraction index of the crystal environment. c is the light velocity and V is the normalized volume. The light-matter coupling can be evaluated on the basis $\left\{|\ldots,n_{\mathbf{q}},\ldots\rangle\otimes|\zeta_X^{\tilde{n},\tilde{\ell},\tilde{m}}\rangle\right\}$. Here, $\{|\ldots,n_{\mathbf{q}},\ldots.\rangle\}$ are the electromagnetic field states in the Fock representation. The solution of the Schrödinger equation for an anisotropic exciton in a solid is as follows

$$\zeta_X^{\tilde{n},\tilde{\ell},\tilde{m}}\left(\mathbf{r_e},\mathbf{r_h}\right)=\Upsilon_{\tilde{n},\tilde{\ell},\tilde{m}}(\mathbf{R_{CM}},\boldsymbol{\rho})u_{c,\mathbf{k}}\left(\mathbf{r_e}\right)u_{v,\mathbf{k}}^{*}\left(\mathbf{r_h}\right) \tag{S25}$$

where $u_{c,\mathbf{k}}\left(\mathbf{r}_e\right)$ and $u_{v,\mathbf{k}}\left(\mathbf{r_h}\right)$ are the Bloch functions of the valence (v) and conduction (c) bands, respectively. $\Upsilon_{\tilde{n},\tilde{\ell},\tilde{m}}(\mathbf{R_{CM}},\boldsymbol{\rho})$ is the envelope wavefunction. In our work, the initial state consists of an excitonic state without a photon $|i\rangle=\left|\zeta_X^{\tilde{n},\tilde{\ell},\tilde{m}}\right\rangle\otimes|0_{\mathbf{q}}\rangle$, while the final state consists of the crystal ground state $|\emptyset\rangle$ with one photon $|f\rangle=|\emptyset\rangle\otimes|1_{\mathbf{q}}\rangle$. The OME can be written as

$$\Big(\langle 1_{\mathbf{q}}|\otimes\langle\emptyset|\Big)\mathbf{A}_{\mathbf{q}}^{+}(\mathbf{r})\cdot\mathbf{p}\Big(|\zeta_X^{\tilde{n},\tilde{\ell},\tilde{m}}\rangle\otimes|0_{\mathbf{q}}\rangle\Big)=\sqrt{\left(\frac{2\pi\hbar c}{n_0\mathbf{q}V}\right)}\bar{F}_{\mathbf{q},c,v}^{\tilde{n},\tilde{\ell},\tilde{m}} \tag{S26}$$

where $\bar{F}_{\mathbf{q},c,v}^{\tilde{n},\tilde{\ell},\tilde{m}}=\boldsymbol{\alpha}_{\mathbf{q}}\cdot\left\langle\emptyset\left|e^{i\mathbf{q}\cdot\mathbf{r}}\mathbf{p}\right|\zeta_X^{\tilde{n},\tilde{\ell},\tilde{m}}\right\rangle$ is the OME between the crystal ground state $|\emptyset\rangle$ and the excited states $|\zeta_X^{\tilde{n},\tilde{\ell},\tilde{m}}\rangle$ corresponding to the direct exciton state in bulk GeS, which is derived from the electron-photon coupling. The linear optical properties of three-dimensional exci-

tons have been investigated theoretically. In fact, the OS of the optical interband transition for exciton states is defined by[42]

$$f^{\alpha_{\mathbf{q}}}_{\tilde{n},\tilde{\ell},\tilde{m}} = \frac{2}{m_0 \hbar \omega_0} \left| \bar{F}^{\tilde{n},\tilde{\ell},\tilde{m}}_{\mathbf{q},c,v} \right|^2 \tag{S27}$$

here, the optical transition frequency is $\omega_0 = |\omega_i - \omega_f| = \omega^X$, with $E^X_{\tilde{n},\tilde{\ell},\tilde{m}} = \hbar\omega^X$. To calculate the OME obtained considering the interaction with the first-order electromagnetic field, it is convenient to work with the Fourier transforms of the envelope wavefunction

$$\zeta^{\tilde{n},\tilde{\ell},\tilde{m}}_X(\mathbf{R_{CM}}, \boldsymbol{\rho}) = \frac{1}{(2\pi)^6} \int\int d\mathbf{K} d\mathbf{k}\, e^{i\left(\mathbf{K}.\mathbf{R_{CM}} + \mathbf{k}.\boldsymbol{\rho}\right)} \bar{\Phi}^{CM}(\mathbf{K}) \bar{\Psi}^{rel}_{\tilde{n},\tilde{\ell},\tilde{m}}(\mathbf{k}) u_{c,\mathbf{k}}(\mathbf{r_e}) u^*_{v,\mathbf{k}}(\mathbf{r_h}) \tag{S28}$$

where the COM and relative wavefunction, in momentum-space, reads

$$\bar{\Phi}^{CM}(\mathbf{K}) = \int e^{i\mathbf{K}.\mathbf{R_{CM}}} \Phi^{CM}(\mathbf{R}_{CM}) d\mathbf{R_{CM}} \tag{S29a}$$

$$\bar{\Psi}^{rel}_{\tilde{n},\tilde{\ell},\tilde{m}}(\mathbf{k}) = \int e^{i\mathbf{k}.\boldsymbol{\rho}} \Psi^{rel}_{\tilde{n},\tilde{\ell},\tilde{m}}(\boldsymbol{\rho}) d\boldsymbol{\rho} \tag{S29b}$$

here, $\mathbf{K} = \mathbf{k}_e + \mathbf{k_h}$ and $\mathbf{k} = \frac{m^h_i \mathbf{k}_e - m^e_i \mathbf{k}_h}{M_{X,i}}$ are the COM and the relative wavevectors, respectively. By considering the following change of variables, $(\mathbf{K}, \mathbf{k}) \Rightarrow (\mathbf{k}_e, \mathbf{k}_h)$, with $d\mathbf{K}d\mathbf{k} = d\mathbf{k}_e d\mathbf{k}_h$, the envelope wavefunction, $\zeta^{\tilde{n},\tilde{\ell},\tilde{m}}_X$, can be written as follows

$$\zeta^{\tilde{n},\tilde{\ell},\tilde{m}}_X(\mathbf{r_e}, \mathbf{r_h}) = \frac{1}{(2\pi)^6} \int\int d\mathbf{k}_e d\mathbf{k}_h e^{i(\mathbf{k_e}\cdot\mathbf{r_e} + \mathbf{k_h}\cdot\mathbf{r_h})} \bar{\Phi}(\mathbf{K}) \bar{\Psi}^{rel}_{\tilde{n},\tilde{\ell},\tilde{m}}(\mathbf{k}) u_{c,\mathbf{k}}(\mathbf{r}_e)\, u^*_{v,\mathbf{k}}(\mathbf{r}_h) \tag{S30}$$

By converting the integral into a sum ($\frac{1}{V}\sum_{\mathbf{k}\in 1BZ} \approx \int_{\mathbf{k}\in 1BZ} \frac{d\mathbf{k}}{(2\pi)^3}$), we can rewrite $\zeta^{\tilde{n},\tilde{\ell},\tilde{m}}_X(\mathbf{r_e}, \mathbf{r_h})$ as follows

$$\zeta^{\tilde{n},\tilde{\ell},\tilde{m}}_X(\mathbf{r_e}, \mathbf{r_h}) = \frac{1}{V^2} \sum_{\mathbf{k}_e\in BZ} \sum_{\mathbf{k}_h\in BZ} e^{i(\mathbf{k}_e\cdot\mathbf{r}_e + \mathbf{k}_h\cdot\mathbf{r}_h)} \bar{\Phi}^{CM}(\mathbf{K}) \bar{\Psi}^{rel}_{\tilde{n},\tilde{\ell},\tilde{m}}(\mathbf{k}) u_{c,\mathbf{k}}(\mathbf{r_e}) \times u^*_{v,\mathbf{k}}(\mathbf{r}_h) \tag{S31}$$

The Bloch functions $u_{c,\mathbf{k}}(\mathbf{r}_e)$, $u^*_{v,\mathbf{k}}(\mathbf{r}_h) = u_{h,-\mathbf{k}}(\mathbf{r}_h)$ vary slowly when $\mathbf{k}_e$ ($\mathbf{k}_h$) vary around

the **k**-points. We can therefore write

$$\zeta_X^{\tilde{n},\tilde{\ell},\tilde{m}}(\mathbf{r_e},\mathbf{r_h}) = \frac{1}{V}\sum_{\mathbf{k}_e,\mathbf{k}_h\in BZ} \bar{\Phi}^{CM}(\mathbf{K})\bar{\Psi}^{rel}_{\tilde{n},\tilde{\ell},\tilde{m}}(\mathbf{k})\Upsilon_{c,\mathbf{k}_e}(\mathbf{r_e}) \times \Upsilon^*_{v,\mathbf{k}_h}(\mathbf{r}_h) \tag{S32}$$

where the electron and hole wavefunctions reads

$$\Upsilon_{c,\mathbf{k}_e}(\mathbf{r}_e) = \frac{1}{\sqrt{V}} e^{i\mathbf{k}_e\cdot\mathbf{r}_e} u_{c,\mathbf{k}_e}(\mathbf{r}_e) \tag{S33a}$$

$$\Upsilon_{v,\mathbf{k}_v}(\mathbf{r}_h) = \frac{1}{\sqrt{V}} e^{i\mathbf{k}_v\cdot\mathbf{r}_h} u_{v,\mathbf{k}_v}(\mathbf{r}_h)\,. \tag{S33b}$$

Here $\mathbf{k}_h = -\mathbf{k}_v$. In fact, the hole state is related to the valence electron state by $\Upsilon_{\mathbf{k}_h}(\mathbf{r}) = \mathcal{K}\Upsilon_{\mathbf{k}_v}(\mathbf{r})$ with $\mathcal{K}$ being the time-reversal operator.[43] By substituting Eq. S30 in Eq. S26, and since $\mathbf{k}_e, \mathbf{k}_h \in$ BZ, the OME reads

$$\bar{F}^{\tilde{n},\tilde{\ell},\tilde{m}}_{\mathbf{q},c,v} = \frac{1}{V}\sum_{\mathbf{k}_e,\mathbf{k}_h} \bar{\Phi}^{CM}(\mathbf{K})\bar{\Psi}^{rel}_{\tilde{n},\tilde{\ell},\tilde{m}}(\mathbf{k}) \left\langle u_{c,\mathbf{k}_e} \left| \alpha_{\mathbf{q}}\cdot\mathbf{p} \right| u_{v,\mathbf{k}_v} \right\rangle \delta_{\mathbf{k}_e,\mathbf{k}_v+\mathbf{q}}. \tag{S34}$$

The COM and relative wavevectors can be rewritten as

$$\begin{cases} \mathbf{K} = \mathbf{k}_e + \mathbf{k}_h = \mathbf{k}_e - \mathbf{k}_v = \mathbf{q} \\ \mathbf{k} = \mathbf{k}_e - \frac{m^{e,i}_{eff}}{M^i_X}\mathbf{q} \end{cases} \tag{S35}$$

Using Eq. S35 and Eq. S34, we can rewrite $\bar{F}^{\tilde{n},\tilde{\ell},\tilde{m}}_{\mathbf{q},c,v}$ as follows

$$\bar{F}^{\tilde{n},\tilde{\ell},\tilde{m}}_{\mathbf{q},c,v} = \frac{1}{V}\sum_{\mathbf{k}_e} \bar{\Phi}^{CM}(\mathbf{q})\bar{\Psi}^{rel}_{\tilde{n},\tilde{\ell},\tilde{m}}(\mathbf{k}_e)\,\alpha_{\mathbf{q}}\cdot\langle u_{c,\mathbf{k}}|\mathbf{p}|u_{v,\mathbf{k}}\rangle \tag{S36}$$

At the scale of $\mathbf{q}$, $\bar{\Phi}^{CM}(\mathbf{q})$ is slowly varying, so $\bar{\Phi}^{CM}(\mathbf{q}) = \bar{\Phi}^{CM}(0)$, hence,

$$\bar{F}^{\tilde{n},\tilde{\ell},\tilde{m}}_{\mathbf{q},c,v} = \frac{1}{V}\bar{\Phi}^{CM}(\mathbf{K}=0)\sum_{\mathbf{k}_e} \bar{\Psi}^{rel}_{\tilde{n},\tilde{\ell},\tilde{m}}(\mathbf{k}_e)\,\alpha_{\mathbf{q}}\cdot\langle u_{c,\mathbf{k}}|\mathbf{p}|u_{v,\mathbf{k}}\rangle \tag{S37}$$

with

$$\frac{1}{V}\sum_{\mathbf{k}_e}\bar{\Psi}^{rel}_{\tilde{n},\tilde{\ell},\tilde{m}}\left(\mathbf{k}_e\right)=\frac{1}{(2\pi)^3}\int d\mathbf{k}_e\bar{\Psi}_{\tilde{n},\tilde{\ell},\tilde{m}}\left(\mathbf{k}_e\right)=V\Psi^{rel}_{\tilde{n},\tilde{\ell},\tilde{m}}(\rho=0) \tag{S38a}$$

$$\bar{\Phi}^{CM}(\mathbf{K}=0)=\int d\mathbf{R}_{\mathbf{CM}}\,\Phi^{CM}(\mathbf{R}_{CM}) \tag{S38b}$$

In the case of bulk GeS in which we assume the exciton COM motion is free and can be described by a plane wavefunction, the OS is rewritten as follows

$$f^{\alpha_{\mathbf{q}}}_{\tilde{n},\tilde{\ell},\tilde{m}}=\frac{2V}{m_0E^X_{\tilde{n},\tilde{\ell},\tilde{m}}}\left|\Psi^{rel}_{\tilde{n},\tilde{\ell},\tilde{m}}(\rho=0)\right|^2\times\left|\langle u_{c,\mathbf{k}}\left|\boldsymbol{\alpha}_{\mathbf{q}}\cdot\mathbf{p}\right|u_{v,\mathbf{k}}\rangle\right|^2. \tag{S39}$$

References

1. Zawadzka, N.; Kipczak, Ł.; Woźniak, T.; Olkowska-Pucko, K.; Grzeszczyk, M.; Babiński, A.; Molas, M. R. Anisotropic Optical and Vibrational Properties of GeS. *Nanomaterials* **2021**, *11*, 3109.

2. O'Donnell, K. P.; Chen, X. Temperature dependence of semiconductor band gaps. *Applied Physics Letters* **1991**, *58*, 2924–2926.

3. Rudin, S.; Reinecke, T. L.; Segall, B. Temperature-dependent exciton linewidths in semiconductors. *Phys. Rev. B* **1990**, *42*, 11218–11231.

4. Arora, A.; Koperski, M.; Nogajewski, K.; Marcus, J.; Faugeras, C.; Potemski, M. Excitonic resonances in thin films of WSe2: from monolayer to bulk material. *Nanoscale* **2015**, *7*, 10421–10429.

5. Molas, M. R.; Nogajewski, K.; Slobodeniuk, A. O.; Binder, J.; Bartos, M.; Potemski, M. The optical response of monolayer, few-layer and bulk tungsten disulfide. *Nanoscale* **2017**, *9*, 13128–13141.

6. Kezerashvili, R. Y.; Tsiklauri, S. M. Trion and biexciton in monolayer transition metal dichalcogenides. *Few-Body Systems* **2017**, *58*, 1–5.

7. Vaclavkova, D.; Wyzula, J.; Nogajewski, K.; Bartos, M.; Slobodeniuk, A.; Faugeras, C.; Potemski, M.; Molas, M. Singlet and triplet trions in WS2 monolayer encapsulated in hexagonal boron nitride. *Nanotechnology* **2018**, *29*, 325705.

8. Yang, J.; Xu, R.; Pei, J.; Myint, Y. W.; Wang, F.; Wang, Z.; Zhang, S.; Yu, Z.; Lu, Y. Optical tuning of exciton and trion emissions in monolayer phosphorene. *Light: Science & Applications* **2015**, *4*, e312–e312.

9. Xu, R.; Zhang, S.; Wang, F.; Yang, J.; Wang, Z.; Pei, J.; Myint, Y. W.; Xing, B.; Yu, Z.; Fu, L., *et al.* Extraordinarily bound quasi-one-dimensional trions in two-dimensional phosphorene atomic semiconductors. *Acs Nano* **2016**, *10*, 2046–2053.

10. Ayari, S.; Quick, M. T.; Owschimikow, N.; Christodoulou, S.; Bertrand, G. H.; Artemyev, M.; Moreels, I.; Woggon, U.; Jaziri, S.; Achtstein, A. W. Tuning trion binding energy and oscillator strength in a laterally finite 2D system: CdSe nanoplatelets as a model system for trion properties. *Nanoscale* **2020**, *12*, 14448–14458.

11. Durnev, M. V.; Glazov, M. M. Excitons and trions in two-dimensional semiconductors based on transition metal dichalcogenides. *Physics-Uspekhi* **2018**, *61*, 825.

12. Van der Donck, M.; Zarenia, M.; Peeters, F. Excitons, trions, and biexcitons in transition-metal dichalcogenides: magnetic-field dependence. *Physical Review B* **2018**, *97*, 195408.

13. Louyer, Y.; Biadala, L.; Trebbia, J.-B.; Fernée, M. J.; Tamarat, P.; Lounis, B. Efficient biexciton emission in elongated CdSe/ZnS nanocrystals. *Nano letters* **2011**, *11*, 4370–4375.

14. Steinhoff, A.; Florian, M.; Singh, A.; Tran, K.; Kolarczik, M.; Helmrich, S.; Achtstein, A. W.; Woggon, U.; Owschimikow, N.; Jahnke, F., *et al.* Biexciton fine structure in monolayer transition metal dichalcogenides. *Nature Physics* **2018**, *14*, 1199–1204.

15. Tonndorf, P.; Schmidt, R.; Schneider, R.; Kern, J.; Buscema, M.; Steele, G. A.; Castellanos-Gomez, A.; van der Zant, H. S.; de Vasconcellos, S. M.; Bratschitsch, R. Single-photon emission from localized excitons in an atomically thin semiconductor. *Optica* **2015**, *2*, 347–352.

16. Wang, G.; Bouet, L.; Lagarde, D.; Vidal, M.; Balocchi, A.; Amand, T.; Marie, X.; Urbaszek, B. Valley dynamics probed through charged and neutral exciton emission in monolayer WSe 2. *Physical Review B* **2014**, *90*, 075413.

17. Zhang, S.; Wang, C.-G.; Li, M.-Y.; Huang, D.; Li, L.-J.; Ji, W.; Wu, S. Defect structure of localized excitons in a WSe 2 monolayer. *Physical review letters* **2017**, *119*, 046101.

18. Pelant, I.; Valenta, J. *Luminescence spectroscopy of semiconductors*; OUP Oxford, 2012.

19. Lin, Z.; Carvalho, B. R.; Kahn, E.; Lv, R.; Rao, R.; Terrones, H.; Pimenta, M. A.; Terrones, M. Defect engineering of two-dimensional transition metal dichalcogenides. *2D Materials* **2016**, *3*, 022002.

20. Singh, A.; Moody, G.; Tran, K.; Scott, M. E.; Overbeck, V.; Berghäuser, G.; Schaibley, J.; Seifert, E. J.; Pleskot, D.; Gabor, N. M., *et al.* Trion formation dynamics in monolayer transition metal dichalcogenides. *Physical Review B* **2016**, *93*, 041401.

21. Sangalli, D.; Berger, J. A.; Attaccalite, C.; Grüning, M.; Romaniello, P. Optical properties of periodic systems within the current-current response framework: Pitfalls and remedies. *Phys. Rev. B* **2017**, *95*, 155203.

22. Rohlfing, M.; Louie, S. G. Electron-Hole Excitations in Semiconductors and Insulators. *Phys. Rev. Lett.* **1998**, *81*, 2312–2315.

23. Molina-Sánchez, A.; Sangalli, D.; Hummer, K.; Marini, A.; Wirtz, L. Effect of spin-orbit interaction on the optical spectra of single-layer, double-layer, and bulk MoS_2. *Phys. Rev. B* **2013**, *88*, 045412.

24. Malone, B. D.; Kaxiras, E. Quasiparticle band structures and interface physics of SnS and GeS. *Phys. Rev. B* **2013**, *87*, 245312.

25. Makinistian, L.; Albanesi, E. First-principles calculations of the band gap and optical properties of germanium sulfide. *Physical Review B* **2006**, *74*, 045206.

26. Oliva, R.; Woźniak, T.; Dybala, F.; Tołłoczko, A.; Kopaczek, J.; Scharoch, P.; Kudrawiec, R. Valley polarization investigation of GeS under high pressure. *Phys. Rev. B* **2020**, *101*, 235205.

27. Castillo-Mussot, M. d.; Vazquez, G. J.; Reyes, J. Variational anisotropic model of Wannier excitons compared with fractional-dimensional space approach. *Revista mexicana de física* **2002**, *48*, 504–507.

28. Schindlmayr, A. Excitons with anisotropic effective mass. *European Journal of Physics* **1997**, *18*, 374.

29. Carré, E.; Sponza, L.; Lusson, A.; Stenger, I.; Gaufrès, É.; Loiseau, A.; Barjon, J. Excitons in bulk black phosphorus evidenced by photoluminescence at low temperature. *2D Materials* **2021**, *8*, 021001.

30. Wirtz, L.; Marini, A.; Gruning, M.; Rubio, A. Excitonic effects in optical absorption and electron-energy loss spectra of hexagonal boron nitride. *arXiv preprint cond-mat/0508421* **2005**,

31. Molina-Sánchez, A.; Sangalli, D.; Hummer, K.; Marini, A.; Wirtz, L. Effect of spin-orbit interaction on the optical spectra of single-layer, double-layer, and bulk MoS2. *Physical Review B* **2013**, *88*, 045412.

32. Kuzuba, T.; Era, K. Nearly Hydrogenic Energy-Levels of Wannier Excitons in Anisotropic Crystals. *Journal of the Physical Society of Japan* **1976**, *40*, 134–139.

33. Baldereschi, A.; Diaz, M. Anisotropy of excitons in semiconductors. *Il Nuovo Cimento B (1965-1970)* **1970**, *68*, 217–229.

34. Dresselhaus, G. Effective mass approximation for excitons. *Journal of Physics and Chemistry of Solids* **1956**, *1*, 14–22.

35. Olsen, T.; Latini, S.; Rasmussen, F.; Thygesen, K. S. Simple screened hydrogen model of excitons in two-dimensional materials. *Physical review letters* **2016**, *116*, 056401.

36. Cudazzo, P.; Tokatly, I. V.; Rubio, A. Dielectric screening in two-dimensional insulators: Implications for excitonic and impurity states in graphane. *Physical Review B* **2011**, *84*, 085406.

37. Keldysh, L. Coulomb interaction in thin semiconductor and semimetal films. *Soviet Journal of Experimental and Theoretical Physics Letters* **1979**, *29*, 658.

38. Chernikov, A.; Berkelbach, T. C.; Hill, H. M.; Rigosi, A.; Li, Y.; Aslan, B.; Reichman, D. R.; Hybertsen, M. S.; Heinz, T. F. Exciton binding energy and nonhydrogenic Rydberg series in monolayer WS2. *Physical review letters* **2014**, *113*, 076802.

39. Rytova, N. S. Screened potential of a point charge in a thin film. *arXiv preprint arXiv:1806.00976* **2018**,

40. Taguchi, S.; Goto, T.; Takeda, M.; Kido, G. Magneto-optical effects of the wannier exciton in a biaxial ZnP2 crystal. I. *Journal of the Physical Society of Japan* **1988**, *57*, 3256–3261.

41. Burstein, E.; Weisbuch, C. *Confined electrons and photons: New physics and applications*; Springer Science & Business Media, 2012; Vol. 340.

42. Stier, O.; Grundmann, M.; Bimberg, D. Electronic and optical properties of strained quantum dots modeled by 8-band k. p theory. *Physical Review B* **1999**, *59*, 5688.

43. Bir, G. L.; Pikus, G. E.; Louvish, D. *Symmetry and strain-induced effects in semiconductors*; Wiley New York, 1974; Vol. 484.